Cell-Based Domain Decomposition for Metasurface Antennas Design

Received 29 November 2025; accepted 3 January 2026. Date of publication 12 January 2026; date of current version 26 March 2026.

*Digital Object Identifier 10.1109/OJAP.2026.3652094*

# Cell-Based Domain Decomposition for Metasurface Antennas Design

**LEONARDO POLLINI [1] (Graduate Student Member, IEEE), MARCELLO ZUCCHI [2] (Member, IEEE), AND GIUSEPPE VECCHI [1] (Life Fellow, IEEE)**

[1]Department of Electronics and Telecommunications, Politecnico di Torino, 10129 Torino, Italy
[2]Advanced Computing, Photonics & Electromagnetics Area, Fondazione LINKS, 10138 Turin, Italy

CORRESPONDING AUTHOR: GIUSEPPE VECCHI (e-mail: giuseppe.vecchi@polito.it)

This work was supported by the European Union – Next Generation EU under the Italian National Recovery and Resilience Plan (NRRP), Mission 4, Component 2, Investment 1.3, CUP E13C22001870001, partnership on "Telecommunications of the Future" (PE00000001 – program "RESTART").

**ABSTRACT** Metasurface design methods typically follow a two-stage approach based on the (surface) Impedance Boundary Condition (IBC) approximation of the macroscopic behaviour of the metasurface. In the first step, the surface impedance profile is optimized to meet the specifications; then, unit-cells are designed to reproduce the impedance profile. Usually, the metasurface geometry is considered continuous and the (equivalent) current can flow everywhere on the surface. In this contribution, we investigate on the impact of the discretization of the optimization domain, and its decomposition to conform to the actual size of the unit-cells in the context of a deterministic current-based optimization method. It is shown that information on the unit-cell size can guarantee better agreement between the resulting IBC and the actual realization with physical unit-cells. Also, optimization convergence is notably faster.

**INDEX TERMS** Antenna synthesis, impedance boundary condition (IBC), metasurface antennas, method of moments (MoM).

## I. INTRODUCTION

IN THE last decade, the use of metasurfaces has seen a rise in popularity for the realization of a wide range of devices: antennas, lenses, polarizers, reflect- and transmit-arrays.

Real-life metasurfaces are electrically large, and composed of tens of thousands of sub-wavelength radiating elements printed on a dielectric substrate; this would make a direct global design of the individual cells exceedingly challenging with current computational resources. For this reason, the most successful design approach follows a two-step hierarchical procedure. Firstly, the macroscopic behavior of the metasurface is modeled as an infinitely thin layer on which an appropriate boundary condition (depending on design parameters) is imposed, which makes analysis and design a computationally affordable task. Then, once the proper distribution of boundary condition parameters is found, the surface is synthesized by realizing suitable sub-wavelength scatterers (usually described by a set of geometrical parameters) that implement the sought-for boundary condition at the macroscopic scale.

The chosen boundary condition varies depending on the properties exhibited by the artificial surface, and on the specific application. In the most general case, the surface can be modeled with a Generalized Sheet Transition Condition (GSTC) [1] or as a Bianisotropic Metasurface (BMS) [2], which encompass magneto-electric coupling at the interface and are suitable to model transmission properties through a surface (e.g., transmitarrays, metalenses, and Huygens' metasurfaces). If only electric coupling is of interest, a simpler but effective model is to consider the metasurface as an Impedance Boundary Condition (IBC) layer. The latter represents the most suitable model in the context of modulated metasurface antennas, in which a surface wave excites the structure and radiation arises from leaky-wave phenomena, and will be the focus of the present work.

The macroscopic design of the IBC profile carries most of the total computational cost: for this reason, different methods have been proposed. For the sake of compactness, we focus here on methods that formulate the design instance

in terms of the equivalent surface current, either exclusively or partially; they subsequently recover the sought-for surface impedance from the optimal current distribution. In particular, 2D methods target geometries that have one invariant axis, allowing a stark reduction in the problem size. Among these, [3] optimizes both the current and the impedance at the same time, with alternating-type optimization; [4], [5] directly enforce the losslessness condition, considering a transmission-type problem. In [6], a multi-layer problem is considered, with an integral equation modeling and pattern-matching requirements. Lastly, of particular interest is the approach first proposed in [7], [8], where the inclusion of surface-waves, which transfer power bound to the surface, allows to achieve passive and lossless beamforming. In [9], fields and currents are expanded in Floquet waves and a proper matching procedure ensures a passive lossless impedance for efficient space- to surface-wave conversion and beamforming.

3D methods, on the other hand, address the design of realistic geometries in space, and are therefore more demanding from the computational point of view. In [10], [11], the authors employ entire-domain basis functions defined on circular and elliptical domains for an efficient solution of the inverse problem, given the objective field in amplitude and phase; they effectively transferred to 3D the surface-wave power balance approach introduced in [7]. In [12] non-radiating surface currents are used to enforce passivity and losslessness in the closely-related design of reflectarrays. A fully automated procedure has been introduced in [13]; it is applicable to arbitrarily shaped surfaces, allows mask-type field constraints, and realization bounds on the IBC values. It was extended in [14] to accommodate for accurate feed modeling.

In this work, we present a method to improve current-based metasurface design by exploiting the intrinsic discrete nature of the surface impedance, which involves local averages of tangential electric and magnetic fields. The proposed approach draws inspiration from the 2D method presented in [15], for the design of reflectarrays, and in [16] by the same author for the general case of composite metasurfaces. Here, in a similar vein, with the aim to improve the modeling of the physical problem at the macroscopic scale, the surface is partitioned into small electrically isolated subdomains (unit-cells) that capture the local behavior of the current. This is in contrast with existing 3D current-based methods [10], [13], where the current is assumed to flow continuously across the surface, with no a priori information about the discrete nature of the underlying lattice in the IBC model used for the design. While the method and findings are general and can be directly applied to any current-based design procedure, in the following we employ the algorithm in [13], that allows to efficiently handle electrically large antennas.

We will present results for two different approaches for the domain decomposition, with comparison to the corresponding continuous current design, showing that the presented cell-aware approach leads to better final results and faster convergence. To the best of the authors' knowledge the approach and results have never been presented in the literature.

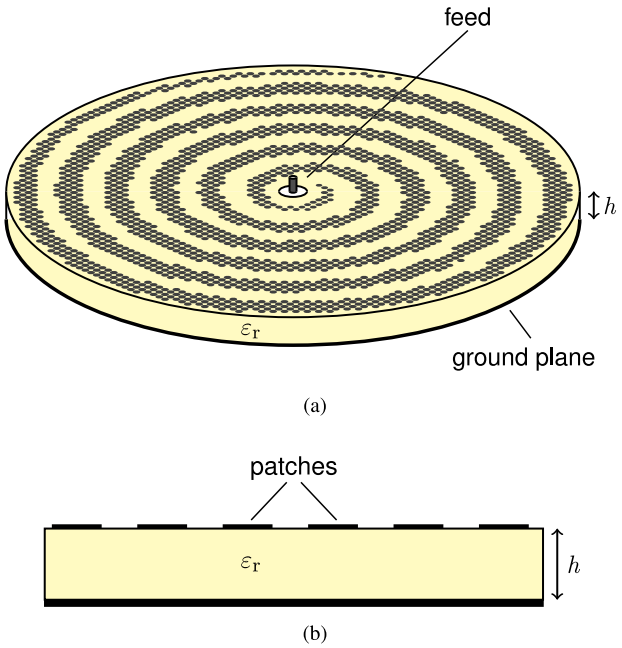


**FIGURE 1.** Layout of a circular metasurface antenna: (a) 3D layout view, (b) cross-section.

## II. BACKGROUND

### A. METASURFACE MODELING

We consider here the case of planar metal texture layers (usually composed of patches), embedded in a dielectric stratification (Fig. 1(a)); while the structure could be complicated (e.g., multiple metalization layers), in the following we will consider the simple case of a single, grounded dielectric layer with a printed metasurface on top of it. The cross section is shown in Fig. 1(b). We will use the following terminology: *unit-cell* refers to the unit surface domain of the periodic lattice (usually square, but in general can also be hexagonal) on which the patterning is based, while *patch* indicates the chosen printed conducting shape inside each cell (in this work we will consider a simple square shape, but it can be any two-dimensional shape fitting inside the cell).

The metasurface fine structure (unit-cell level) is approximated via the Impedance Boundary Condition (IBC), which entails dealing with local *averages* of fields in the metasurface plane [1], [17], [18]. In particular, we will employ the so-called "transparent" version of the IBC [19] that has been shown to be more stable and better represent the spatial dispersion of the layered medium. With this approximation, the unit-cell texturing is represented as an infinitesimally thin IBC layer, which establishes a linear relationship between the average tangential electric field across the

surface and the (averaged) jump in the tangential magnetic field:

$$\boldsymbol{E}_{\tan} = \overline{\overline{\boldsymbol{Z}}} \cdot \left[\hat{\boldsymbol{n}} \times \left(\boldsymbol{H}^{+} - \boldsymbol{H}^{-}\right)\right], \tag{1}$$

where $\overline{\overline{\boldsymbol{Z}}}$ is the local surface impedance, which (typically) varies on the surface, and in general exhibits tensor properties. The magnetic field on the two sides of the surface is denoted as $\boldsymbol{H}^{\pm}$ and the unit vector $\hat{\boldsymbol{n}}$ normal to the surface is directed toward the "+" side. In this contribution we will assume the impedance to be scalar, i.e., $\overline{\overline{\boldsymbol{Z}}} = Z\overline{\overline{\boldsymbol{I}}}$. The use of scalar or tensor impedance impacts the design algorithm, but not the findings of this study. Under the scalar impedance assumption, (1) can be rewritten as:

$$\boldsymbol{E}_{\tan} = Z\boldsymbol{J}, \tag{2}$$

having defined the equivalent surface current,

$$\boldsymbol{J} = \hat{\boldsymbol{n}} \times \left(\boldsymbol{H}^{+} - \boldsymbol{H}^{-}\right). \tag{3}$$

Enforcement of the IBC leads to the *Electric Field Integral Equation* (EFIE-IBC),

$$\boldsymbol{E}_{\text{inc}} + \mathcal{L}\boldsymbol{J} = Z\boldsymbol{J}, \tag{4}$$

where $\boldsymbol{E}_{\text{inc}}$ is the incident source field and $\mathcal{L}$ is the Electric Field Integral Operator for the layered medium.

The EFIE-IBC is discretized via the standard Method of Moments based on a triangular mesh of the antenna surface and on the use of Rao-Wilton-Glisson (RWG) basis functions [20] for representing the surface current,

$$\boldsymbol{J}(\boldsymbol{r}) = \sum_{n=1}^{N} I_n \boldsymbol{\Lambda}_n(\boldsymbol{r}). \tag{5}$$

Use of Galerkin testing leads to the linear system

$$\mathsf{V}_{\text{inc}} + \mathbf{L}\mathsf{I} = \mathbf{Z}\mathsf{I}, \tag{6}$$

with the array $\mathsf{I}$ containing the RWG coefficients and the other quantities defined as

$$(\mathsf{V}_{\text{inc}})_m = \langle \boldsymbol{\Lambda}_m, \boldsymbol{E}_{\text{inc}} \rangle, \tag{7}$$

$$(\mathbf{L})_{mn} = \langle \boldsymbol{\Lambda}_m, \mathcal{L}\boldsymbol{\Lambda}_n \rangle, \tag{8}$$

$$(\mathbf{Z})_{mn} = \langle \boldsymbol{\Lambda}_m, Z\boldsymbol{\Lambda}_n \rangle, \tag{9}$$

where the bilinear form is defined as

$$\langle \boldsymbol{a}, \boldsymbol{b} \rangle = \iint_S \boldsymbol{a} \cdot \boldsymbol{b}\, dS. \tag{10}$$

### B. CURRENT-BASED OPTIMIZATION ALGORITHM

The current-based design method used in the present work is the one described in [13], [14]. Once the geometry of the surface and the source have been defined, the design problem is formulated as the unconstrained minimization of a non-convex objective function. This function is defined as the sum of *realizability* and *radiation* constraints, defined locally over the surface and on a grid of points in the far field, respectively. All the constraint functionals are rearranged in such a way that they are explicitly dependent on the current only. Then a Non-Linear Conjugate Gradient (NLCG) algorithm is used to minimize the resulting objective function:

$$\mathsf{I}^{\star} = \underset{\mathsf{I} \in \mathbb{C}^N}{\arg\min} (f_{\text{rlz}}(\mathsf{I}) + f_{\text{rad}}(\mathsf{I})), \tag{11}$$

where $\mathsf{I}^{\star}$ is the array of the optimized current coefficients. The definition of the individual terms of functions $f_{\text{rlz}}$ and $f_{\text{rad}}$ is given in App. A (more details can be found in [13]). The method features an efficient gradient evaluation by exploiting fast matrix-vector product routines designed for electromagnetic analysis. Additionally, it employs a global piecewise polynomial line-search, enabling the practical design of large-scale antennas.

## III. IMPEDANCE AND GRANULARITY

### A. SURFACE IMPEDANCE

The IBC approximation summarized in Section II-A implies an averaging of the involved tangential fields along the metasurface. The homogenizing, spatially averaging nature of the surface impedance is defined in several ways in the literature [1], [17], [18].

Here, we will address the averaging process starting from the EFIE-IBC (6), that constitutes the model equation for metasurface design; in particular, we will adopt the perspective of current-based methods (described in Section II-B). In all these methods, the impedance is derived (only) at the end of the optimization process, when a suitable surface current has been obtained, via the EFIE-IBC (6). Unlike in the analysis problem, where $Z$ is assigned and $\boldsymbol{J}$ is unknown, in this case $\boldsymbol{J}$ is considered known (as the result of the optimization process), and $Z$ is to be found.

In [13], the impedance retrieval was outlined in a general setting, that will be repeated here for ease of reference. By representing the spatial variation of the impedance $Z(\boldsymbol{r})$ via a set of chosen expansion functions $\psi_\ell(\boldsymbol{r})$,

$$Z(\boldsymbol{r}, \mathsf{c}) = \sum_{\ell=1}^{L} c_\ell\, \psi_\ell(\boldsymbol{r}), \tag{12}$$

where $L$ is the total number of functions considered. The coefficients $c_\ell$ can be found by enforcing that they minimize the $L^2$-norm error of the IBC boundary condition (2), i.e.,

$$\hat{\mathsf{c}} = \underset{\mathsf{c} \in \mathbb{C}^L}{\arg\min} \|\boldsymbol{E}_{\tan} - Z(\mathsf{c})\boldsymbol{J}\|^2. \tag{13}$$

where the dependence on the position has been omitted for clarity. For the most relevant case of piecewise-constant impedance the expansion functions $\psi_\ell$ are defined as

$$\psi_\ell(\boldsymbol{r}) = \begin{cases} 1, & \text{if } \boldsymbol{r} \in S_\ell \\ 0, & \text{otherwise} \end{cases} \tag{14}$$

where the domains $S_\ell$ of each expansion function are disjoint. By substituting the expansion (12) with the choice (14) inside (13), the function to minimize is convex with respect to the impedance coefficients. By setting to zero its first derivative with respect to the real and imaginary part of the

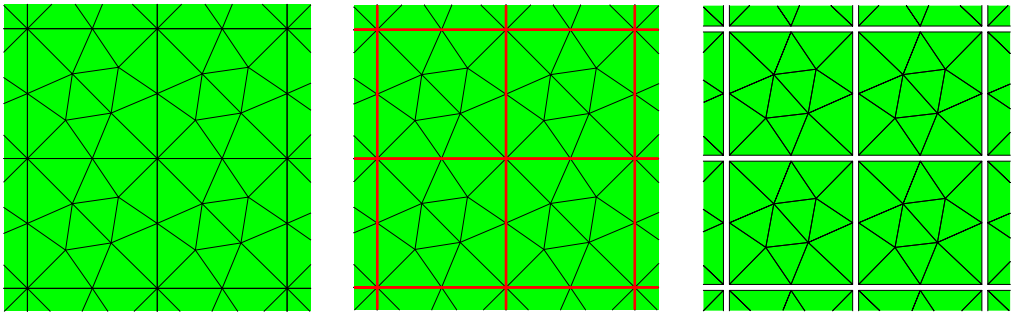


**FIGURE 2.** Different discretization options considered: (a) *Continuous* – the discretization conforms to the unit-cell boundaries, and the current is free to flow in the whole domain (Section IV-A); (b) *Domain decomposition – unit-cell domains* – the discretization conforms to the unit-cell boundaries, but the current is not allowed to flow across unit-cell boundaries (Section IV-B), where the red lines indicate electrical isolation; (c) *Domain decomposition – separated domains* – the discretization accounts for a physical gap between neighboring domains (Section IV-C).

coefficients, we arrive at the analytic solution for the optimal impedance coefficients:

$$\hat{c}_\ell = \frac{\langle \boldsymbol{E}_{\tan}, \boldsymbol{J}^* \rangle_{\mathcal{S}_\ell}}{\|\boldsymbol{J}\|^2_{\mathcal{S}_\ell}}, \tag{15}$$

where the subscript $\mathcal{S}_\ell$ indicates that the inner product integration is over the $\ell$-th domain.

In [13] the domains $S_\ell$ were chosen to coincide with the mesh triangles, resulting in a finely varying impedance. In view of the present endeavor, we assume the impedance to be constant over each unit-cell, consistent with its physical averaged nature. Namely, the domains $\mathcal{S}_\ell$ correspond to the *unit-cells* of the metasurface, as will be detailed in the next section.

### B. CELL-BASED DOMAIN DECOMPOSITION

The conventional application of the EFIE-IBC model (4) implies the flow of (equivalent) surface current $\boldsymbol{J}$ across the entire 2D domain, with the effect of disjoint conductive elements (metal patches) modeled as a continuum of (purely reactive) surface impedance. An alternative view of the model arises by considering the unit-cells as disjoint, preventing the flow of current across neighboring cells; this alternative view was introduced in [15] for 1D problems and generalized to 2D problems in [16].

Here, we will compare the two models and consider different embodiments of the latter approach. Using common terminology in computational electromagnetics, we will refer to this approach as "Domain Decomposition" (DD), and introduce the term "Cell-based Domain Decomposition" to emphasize that the sub-domains are physically associated with the unit-cells.

Within the current-based inverse-design strategy adopted here, the cell-based DD approach relaxes the constraints on the impedance profile, accommodating rapid variations that would otherwise hinder the convergence of the numerical solution. Consequently, the choice of isolated cells ensures that the inverse-design problem is better conditioned under physically realistic constraints, resulting in faster convergence and more robust solutions.

The simplest way to implement the DD model is to consider completely disjoint subdomains within each unit-cell, separated by the minimum distance between metal elements, usually dictated by the tolerances of the manufacturing process; this is seen, for example, in Fig. 2(c). A less obvious approach is indicated in Fig. 2(b); the mesh is first defined to conform to the unit-cell (on a square lattice in our case). Next, the RWG basis functions that cross the boundaries between adjacent cells are removed, thus preventing the flow of currents in a manner analogous to meshing physically disjoint sub-domains.

For reference, we will also show results for the case of a classical continuous mesh (Fig.2(a)). To summarize, the discretization options that we will consider are depicted in Fig. 2:

(a) *Continuous*: the mesh conforms to the unit-cells, and the current can flow everywhere across the surface;
(b) *Domain decomposition – unit-cell domains*: the mesh conforms to the unit-cells, and the current is prevented to cross unit-cell boundaries, which are touching;
(c) *Domain decomposition – separated domains*: the meshed domains are physically separated by a small gap (chosen equal to the minimum manufacturing tolerance of the employed technology).

### C. UNIT-CELL PATCH DESIGN

The patch design for each unit-cell, as is common practice, will be based on a local periodicity approximation to compute the corresponding impedance value [21]. We will consider a square lattice with periodicity $h$, consistent with the grid used in the inverse-design. The candidate patch geometries have a pre-defined geometry defined in terms of a small set of parameters (see Fig. 3 for the case with square patches); in the scalar case only one such parameter is necessary (e.g., the side length $L$ of a square patch).

Once the desired impedance (reactance) values for each unit-cell is determined through the macroscopic inverse-design step, the corresponding patch geometry is selected from a precomputed database to best match the target

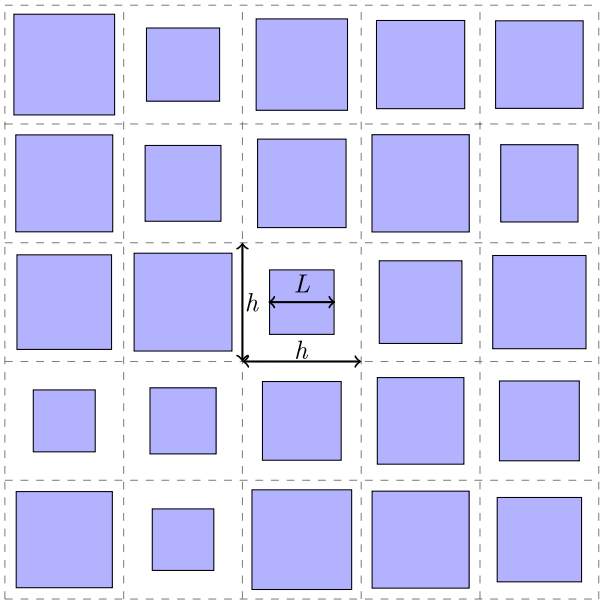


**FIGURE 3.** Example of a metasurface layout with square patches of varying size. Dashed lines mark the boundaries of the lattice *unit-cells*. We notice that, for illustration purposes, the figure shows a square lattice with square patches, although the shape of the patches is arbitrary and is not restricted to squares.

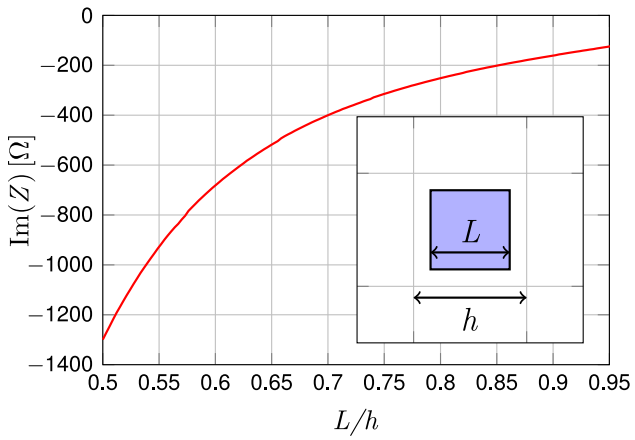


**FIGURE 4.** Square patch database used in this work: the relationship between the square side length and the corresponding impedance is obtained from scattering simulations with periodic approximation, through a parameter sweep over the square side length $L$. The lattice period is $h = \lambda/6$ at a frequency $f = 23$ GHz.

impedance. In the case of square patches, this is simply obtained by inverting the relationship in Fig. 4, which connects the side length of the square patch to the corresponding impedance. The impedance values were obtained with a periodic solver and a parameter sweep over the square patch side length.

## IV. APPLICATION TO CIRCULAR MTS ANTENNA DESIGN

The proposed Domain Decomposition (DD) approach has been verified by carrying out the design of a circular metasurface antenna, from the current-based inverse design to the final layout of the patches. We consider square patches for the synthesis of the impedance. For this purpose, we employed a database built with an in-house code with lattice periodicity $h = \lambda/6$ and a parameter sweep varying from $L = h/2$ to $L = h - \text{tol}$, where $\text{tol} = 100\mu\text{m}$ takes into account the fabrication tolerances. We chose an operational frequency of 23 GHz, for an antenna of diameter $d = 156.4$ mm $\approx 12\lambda$, placed on a grounded dielectric slab with $\varepsilon_r = 3.34$ and thickness $h = 0.508$ mm. The mesh size used for all the presented cases is $\approx \lambda_0/12$. The antenna is excited by a central vertical pin radiating a cylindrical $\text{TM}_0$ surface wave.

The bounds on the reactance in the current-based design have been set, respectively to the minimum and maximum value of impedance of the unit-cells database (Fig. 4), which correspond to capacitive values. Consistent with the chosen square patches, that exhibit a scalar impedance behaviour, we require the impedance to be scalar. As customary, we also imposed local losslessness. The objective was to synthesize a circularly polarized pencil beam radiation pattern, with gain maximization in the main beam and side-lobes level below −20 dB. The definitions of the corresponding terms in the objective function are given in App. A. For this design instance, we considered the three discretization strategies outlined in Section III-B. For the iterative optimization, the maximum number of iterations in all cases was set to 1000.

After the optimization of the current, the impedance for each unit-cell is retrieved as explained in (15) and any residual real part of the impedance, if present, is set to zero. Additionally, unit cells with very low average current magnitudes (i.e., below 1% of the global average) are modeled as open-circuit conditions in impedance terms. In such cases, no patch is placed in the corresponding unit-cell.

For each discretization, we will compare the radiation patterns of the inverse-designed current (labeled *optimized*), of the solution of the corresponding integral equation with the retrieved impedance (*EFIE-IBC*), and of the solution of the final layout with patches (*patches*).

### A. CASE (A): CONTINUOUS

The first case involves a classical, continuous mesh conforming to the underlying unit-cell lattice. The resulting domain consists of 4 044 unit-cells, meshed with a mesh size of $\approx \lambda_0/12$, for a total number of RWG $N = 84\,620$.

The designed impedance distribution has reactance values between $-163\,\text{j}\Omega$ and $-114\,\text{j}\Omega$ (Fig. 5(a)), as well as the radiation patterns, shown in Fig. 6. The maximum directivity is $D = 30.4$ dB for the optimized current distribution, $D = 26$ dB after the reconstruction of the impedance and $D = 25.5$ dB for the final design, respectively. The aperture efficiency follows the same trend, being 78%, 28% and 25%, respectively for the three cases.

### B. CASE (B): DOMAIN DECOMPOSITION—UNIT-CELL DOMAINS

While the first case followed the classical MTS design approach, in which the current is free to flow all over the surface, in this second case we isolate the unit-cells by removing the basis functions across their boundaries. To allow a direct comparison of the results with the previous

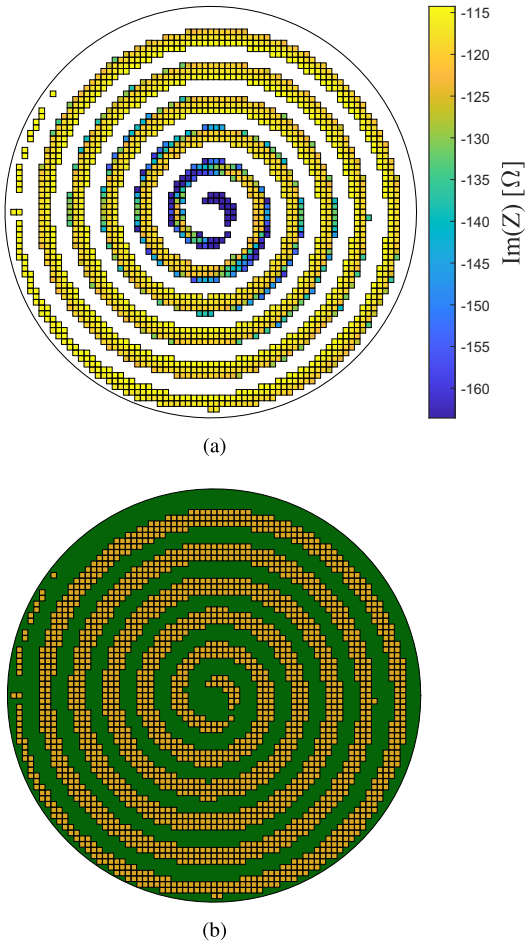


**FIGURE 5.** ***Continuous*** **design: (a) optimized impedance profile (white areas correspond to an open circuit condition), (b) final patch layout.**

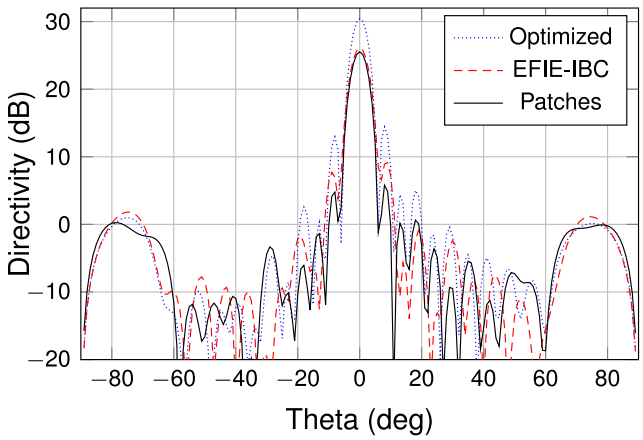


**FIGURE 6.** ***Continuous*** **design: far-field co-polarization directivity comparison in the plane cut $\varphi = 0^\circ$. Optimized current (*blue dotted*), direct EFIE-IBC solution (*red dashed*) and final layout with square patches (*black solid*).**

cases, we used the same mesh as in Section IV-A. With the discontinuity of the subdomains, the total number of RWG functions is $N = 68\,748$, with a 23% reduction in the number of unknowns with respect to the continuous case of the previous section.

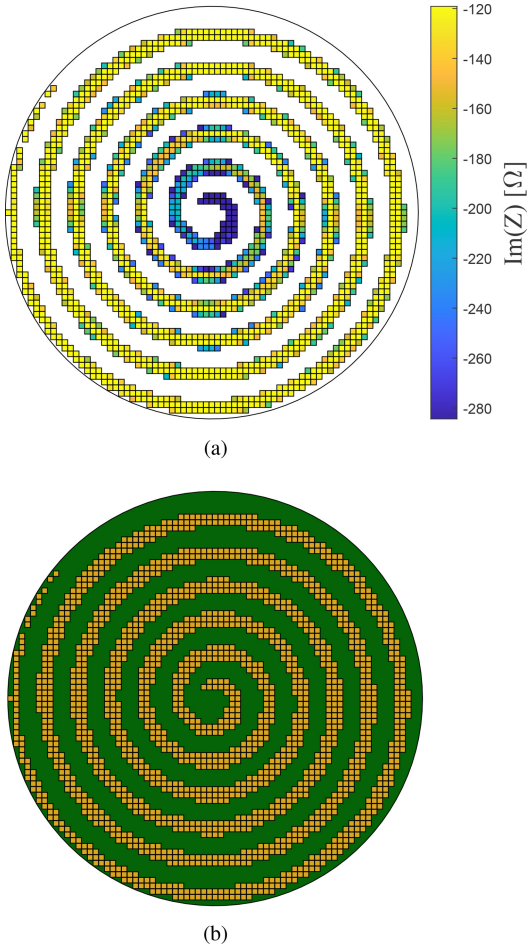


**FIGURE 7.** ***Domain Decomposition – unit-cell domains*** **design: (a) optimized impedance profile (white areas correspond to an open circuit condition), (b) final patch layout.**

In this case the reactance values lie between $-285\,\mathrm{j}\Omega$ and $-118\,\mathrm{j}\Omega$ (Fig. 7(a)). The computational time per iteration is 5 s. Compared to the continuous design, the cell-level impedance granularity introduces a significant reduction in the optimized directivity pattern in Fig. 8, with a directivity at broadside of $D = 26$ dB. However, in this case the EFIE-IBC and the final layout patterns closely match the optimized one, with a maximum directivity of $D = 26.1$ dB and $D = 25.7$ dB, respectively, corresponding to aperture efficiency values respectively of 28%, 28.1% and 27.8%. This shows a noticeable increase in the reliability and robustness of the optimization process when the domain decomposition is introduced.

### C. CASE (C): DOMAIN DECOMPOSITION—SEPARATED DOMAINS

The last case is an extension of the concept of domain decomposition that takes into account the presence of a physical gap between adjacent unit-cells (typical of the final layout with patches) directly in the current optimization phase. We remark that this gap is not related to the final layout with different patch shapes, but is a constant

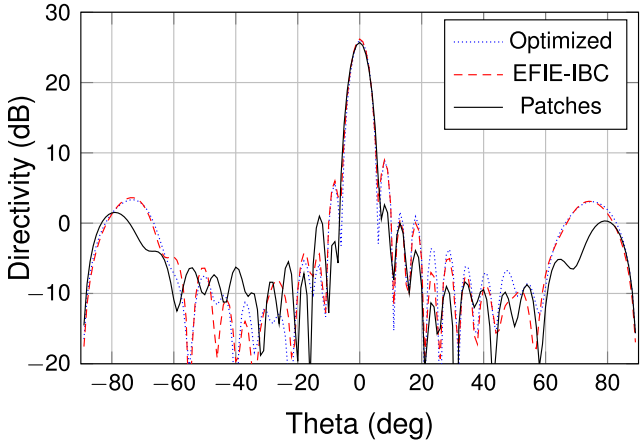


**FIGURE 8.** ***Domain Decomposition – unit-cell domains*** **design: far-field co-polarization directivity comparison in the plane cut $\varphi = 0°$. Optimized current (*blue dotted*), direct EFIE-IBC solution (*red dashed*) and final layout with square patches (*black solid*).**

separation that models the minimum physical separation between each unit-cell radiating surface (i.e., where current is potentially allowed to flow). In this case, the gap was chosen as $100\mu$m, consistent with the fabrication tolerances of printed circuit technology. The total number of RWG functions is the same as in the previous case, since the total number of triangles is the same. Also the computational time is the same as before.

In this case the reactance values lie between $-264\,\mathrm{j}\Omega$ and $-118\,\mathrm{j}\Omega$ (Fig. 9(a)), corresponding to patches in the database with $L/h$ in the range of 0.79–0.95 (Fig. 4). Similarly to the previous case with unit-cell domains, the directivity is practically the same for the optimized current and the EFIE-IBC and final layout, with values of $D = 25.7$ dB, $D = 26$ dB and $D = 25.7$ dB, respectively (Fig.10). The corresponding aperture efficiencies are 27.8%, 28% and 27.8%.

### D. DISCUSSION

From the presented results—particularly the comparison between the optimized radiation patterns and those obtained from the impedance solution and final patch layout—it can be concluded that the Domain Decomposition approach provides significant improvements in both the accuracy and the convergence rate of the inverse-design procedure.

By incorporating information on the unit-cell isolated structure directly into the current optimization problem, it is able to provide a more accurate estimation of the achievable radiation performance after unit-cell implementation.

This additional information leads to a reduction in the effective number of degrees of freedom, which improves the numerical conditioning of the current and impedance solutions. As a consequence, the convergence rate is also greatly improved (Fig. 11): indeed, after only 50 iterations the optimized solution already provides an extremely precise estimation of the final antenna performances.

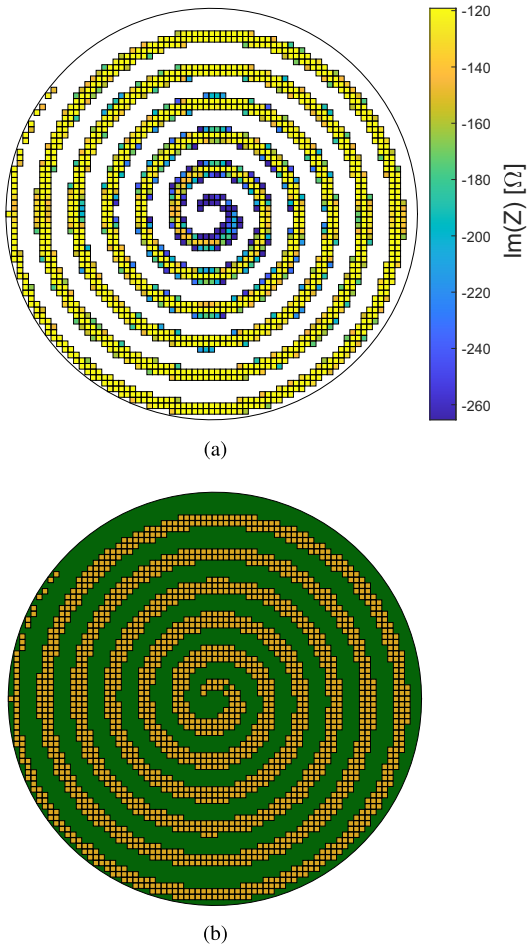


**FIGURE 9.** ***Domain Decomposition – separated domains*** **design: (a) optimized impedance profile (white areas correspond to an open circuit condition), (b) final patch layout.**

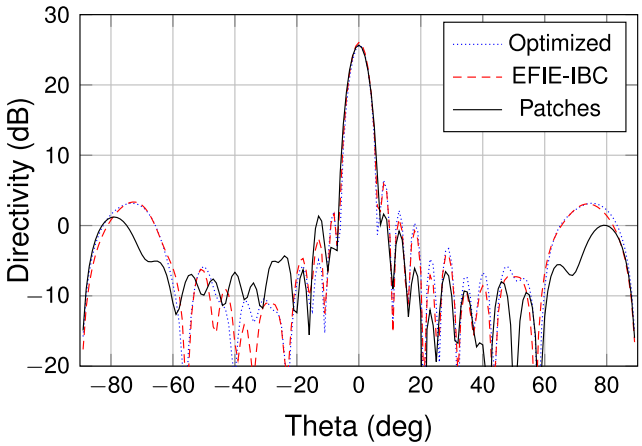


**FIGURE 10.** ***Domain Decomposition – separated domains*** **design: far-field co-polarization directivity comparison in the plane cut $\varphi = 0°$. Optimized current (*blue dotted*), direct EFIE-IBC solution (*red dashed*) and final layout with square patches (*black solid*).**

Finally, the introduction of a physical gap between separated domains does not appear to improve the results significantly with respect to simple unit-cell DD. As such,

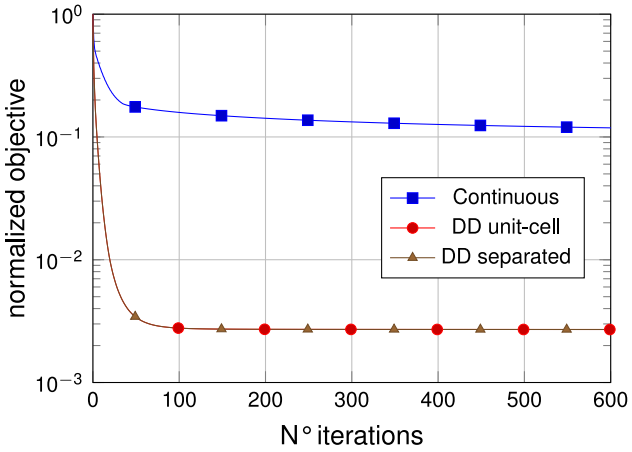


**FIGURE 11.** Convergence rate for each discretization approach: continuous (*squares*), DD with unit-cell domains (*circles*), and DD with separated domains and a physical gap of $100\mu$m (*triangles*).

it looks like the electrical isolation obtained by removing basis functions across cells boundaries is enough to guarantee sufficient robustness.

## V. CONCLUSION

We have presented a benchmark between the usual current-based metasurface design, where the optimization domain is unaware of the underlying structure of the unit-cell lattice, and a new approach based on a unit-cell partitioning of the domain. Continuous and isolated square unit-cells have been considered for the design of a circular metasurface antenna. Square patches were chosen for the synthesis of the impedance.

The proposed domain-decomposition approach offers greater reliability, allowing better assessment of the achievable performances after the current optimization phase, compared to the classical continuous approach. Moreover, convergence is faster thanks to the better conditioning achieved by the reduced number of degrees of freedom for the current.

## APPENDIX A
## OBJECTIVE FUNCTION FOR CURRENT OPTIMIZATION

The objective function for the current-based optimization is composed of two terms: the *realizability* and *radiated field* functionals. In the following, we will summarize definition for both these terms.

The realizability cost function for the IBC includes the conditions of passivity and losslessness ("act"), scalarity ("scal"), and upper/lower impedance bounds ("imp"):

$$f_{\mathrm{rlz}} = w^{\mathrm{act}}\rho^{\mathrm{act}} + w^{\mathrm{scal}}\rho^{\mathrm{scal}} + w^{\mathrm{imp}}\rho^{\mathrm{imp}}. \tag{16}$$

Each of these functionals in turn is expressed as a sum of local functionals defined over individual cells,

$$\rho = \frac{1}{N_{\mathrm{cell}}}\sum_{i=1}^{N_{\mathrm{cell}}}\rho_i. \tag{17}$$

These local functionals are defined as follows:

$$\rho_i^{\mathrm{act}} = \mathcal{P}_i{}^2, \tag{18}$$

$$\rho_i^{\mathrm{scal}} = \mathcal{E}_i\,\mathcal{J}_i - \left(\mathcal{P}_i{}^2 + \mathcal{Q}_i{}^2\right), \tag{19}$$

$$\rho_i^{\mathrm{imp}} = \mathrm{r}^2(X_{\mathrm{L}}\,\mathcal{J}_i - \mathcal{Q}_i) + \mathrm{r}^2(\mathcal{Q}_i - X_{\mathrm{U}}\,\mathcal{J}_i), \tag{20}$$

where $\mathrm{r}(x) = \max(x, 0)$, $X_{\mathrm{L}}$ and $X_{\mathrm{U}}$ denote the lower and upper bounds on the realizable reactance values, respectively, and

$$\mathcal{P}_i = \frac{1}{A_i}\,\mathrm{Re}\iint_{\mathcal{S}_i}\boldsymbol{E}_{\tan}\cdot\boldsymbol{J}^*\,\mathrm{d}S, \tag{21}$$

$$\mathcal{Q}_i = \frac{1}{A_i}\,\mathrm{Im}\iint_{\mathcal{S}_i}\boldsymbol{E}_{\tan}\cdot\boldsymbol{J}^*\,\mathrm{d}S, \tag{22}$$

$$\mathcal{J}_i = \frac{1}{A_i}\iint_{\mathcal{S}_i}|\boldsymbol{J}|^2\,\mathrm{d}S, \tag{23}$$

$$\mathcal{E}_i = \frac{1}{A_i}\iint_{\mathcal{S}_i}|\boldsymbol{E}_{\tan}|^2\,\mathrm{d}S, \tag{24}$$

where $A_i$ is the surface area of the $i$-th cell, $\boldsymbol{J}$ is the surface equivalent current and $\boldsymbol{E}_{\tan}$ is the total electric field tangential to the antenna surface.

Likewise, the radiated field cost functional is defined as

$$f_{\mathrm{rad}} = w^{\mathrm{co}}\rho^{\mathrm{co}} + w^{\mathrm{cx}}\rho^{\mathrm{cx}} + w^{\mathrm{tot}}\rho^{\mathrm{tot}}, \tag{25}$$

where "co" and "cx" refer to co- and cross-polarization, respectively, and "tot" to the total magnitude of the radiated field. Each of these functionals is given by the sum of terms over all considered far field directions:

$$\rho = \frac{1}{N_{\mathrm{ff}}}\sum_{j=1}^{N_{\mathrm{ff}}}\rho_j, \tag{26}$$

with the index $j = 1, \ldots, N_{\mathrm{ff}}$ representing the far field direction $(\theta_j, \phi_j)$. Below are the definitions of each term:

$$\rho_j^{\mathrm{co}} = \mathrm{r}^2\left(M_{\mathrm{L}}^{\mathrm{co}}j - F_j^{\mathrm{co}}\right) + \mathrm{r}^2\left(F_j^{\mathrm{co}} - M_{\mathrm{U}}^{\mathrm{co}}j\right), \tag{27}$$

$$\rho_j^{\mathrm{cx}} = \mathrm{r}^2\left(F_j^{\mathrm{cx}} - M_j^{\mathrm{cx}}\right), \tag{28}$$

$$\rho_j^{\mathrm{tot}} = \mathrm{r}^2\left(F_j^{\mathrm{tot}} - M_j^{\mathrm{tot}}\right), \tag{29}$$

with

$$F_j^{\mathrm{co}} = \left|E_j^{\mathrm{co}}\right|^2, \tag{30}$$

$$F_j^{\mathrm{cx}} = \left|E_j^{\mathrm{cx}}\right|^2, \tag{31}$$

$$F_j^{\mathrm{tot}} = \left|E_j^{\mathrm{co}}\right|^2 + \left|E_j^{\mathrm{cx}}\right|^2. \tag{32}$$

where $E_j^{\mathrm{co}}$ and $E_j^{\mathrm{cx}}$ are the co- and cross-polarization components of the far electric field in the $j$-th direction.

## REFERENCES

[1] E. F. Kuester, M. A. Mohamed, M. Piket-May, and C. L. Holloway, "Averaged transition conditions for electromagnetic fields at a metafilm," *IEEE Trans. Antennas Propag.*, vol. 51, no. 10, pp. 2641–2651, Oct. 2003.

[2] V. S. Asadchy, A. Díaz-Rubio, and S. A. Tretyakov, "Bianisotropic metasurfaces: physics and applications," *Nanophotonics*, vol. 7, no. 6, pp. 1069–1094, 2018.

[3] S. Pearson and S. V. Hum, "Optimization of electromagnetic metasurface parameters satisfying far-field criteria," *IEEE Trans. Antennas Propag.*, vol. 70, no. 5, pp. 3477–3488, May 2022.
[4] T. Brown, Y. Vahabzadeh, C. Caloz, and P. Mojabi, "Electromagnetic inversion with local power conservation for metasurface design," *IEEE Antennas Wireless Propag. Lett.*, vol. 19, pp. 1291–1295, 2020.
[5] T. Brown and P. Mojabi, "Cascaded metasurface design using electromagnetic inversion with gradient-based optimization," *IEEE Trans. Antennas Propag.*, vol. 70, no. 3, pp. 2033–2045, Mar. 2022.
[6] J. Budhu, E. Michielssen, and A. Grbic, "The design of dual band stacked metasurfaces using integral equations," *IEEE Trans. Antennas Propag.*, vol. 70, no. 6, pp. 4576–4588, Jun. 2022.
[7] A. Epstein and G. V. Eleftheriades, "Synthesis of passive lossless metasurfaces using auxiliary fields for reflectionless beam splitting and perfect reflection," *Phys. Rev. Lett.*, vol. 117, no. 25, Dec. 2016, Art. no. 256103.
[8] V. G. Ataloglou and G. V. Eleftheriades, "Arbitrary wave transformations with huygens' metasurfaces through surface-wave optimization," *IEEE Antennas Wireless Propag. Lett.*, vol. 20, pp. 1750–1754, 2021.
[9] T. Arshed, S. Maci, and E. Martini, "Direct synthesis of metasurfaces for efficient space- to surface-wave conversion and beamforming," *IEEE Trans. Antennas Propag.*, vol. 72, no. 10, pp. 7793–7806, Oct. 2024.
[10] M. Bodehou, C. Craeye, E. Martini, and I. Huynen, "A quasi-direct method for the surface impedance design of modulated metasurface antennas," *IEEE Trans. Antennas Propag.*, vol. 67, no. 1, pp. 24–36, Jan. 2019.
[11] M. Bodehou, C. Craeye, and I. Huynen, "Electric field integral equation-based synthesis of elliptical-domain metasurface antennas," *IEEE Trans. Antennas Propag.*, vol. 67, no. 2, pp. 1270–1274, Feb. 2019.
[12] M. Salucci, A. Gelmini, G. Oliveri, N. Anselmi, and A. Massa, "Synthesis of shaped beam reflectarrays with constrained geometry by exploiting nonradiating surface currents," *IEEE Trans. Antennas Propag.*, vol. 66, no. 11, pp. 5805–5817, Nov. 2018.
[13] M. Zucchi, F. Vernì, M. Righero, and G. Vecchi, "Current based automated design of realizable metasurface antennas with arbitrary pattern constraints," *IEEE Trans. Antennas Propag.*, vol. 71, no. 6, pp. 4888–4902, Jun. 2023.
[14] L. Teodorani, M. Zucchi, and G. Vecchi, "Generalized deterministic automated design of metasurface antennas with 3-D feeding structures," *IEEE Trans. Antennas Propag.*, vol. 72, no. 11, pp. 8135–8150, Nov. 2024.
[15] J. Budhu and A. Grbic, "Perfectly reflecting metasurface reflectarrays: Mutual coupling modeling between unique elements through homogenization," *IEEE Trans. Antennas Propag.*, vol. 69, no. 1, pp. 122–134, Jan. 2021.
[16] J. Budhu and S. Xu, "An SIE-GSTC formulation for 3D composite metasurface analysis," in *Proc. IEEE Int. Symp. Antennas Propag.*, 2024, pp. 1505–1506.
[17] B. H. Fong, J. S. Colburn, J. J. Ottusch, J. L. Visher, and D. F. Sievenpiper, "Scalar and tensor holographic artificial impedance surfaces," *IEEE Trans. Antennas Propag.*, vol. 58, no. 10, pp. 3212–3221, Oct. 2010.
[18] C. R. Simovski, "On electromagnetic characterization and homogenization of nanostructured metamaterials," *J. Optics*, vol. 13, no. 1, Nov. 2010, Art. no. 13001.
[19] M. A. Francavilla, E. Martini, S. Maci, and G. Vecchi, "On the numerical simulation of metasurfaces with impedance boundary condition integral equations," *IEEE Trans. Antennas Propag.*, vol. 63, no. 5, pp. 2153–2161, May 2015.
[20] S. Rao, D. Wilton, and A. Glisson, "Electromagnetic scattering by surfaces of arbitrary shape," *IEEE Trans. Antennas Propag.*, vol. 30, no. 3, pp. 409–418, May 1982.
[21] A. M. Patel and A. Grbic, "Effective surface impedance of a printed-circuit tensor impedance surface (PCTIS)," *IEEE Trans. Microw. Theory Tech.*, vol. 61, no. 4, pp. 1403–1413, Apr. 2013.

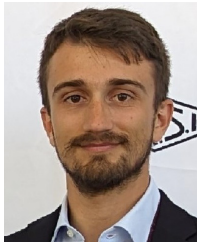

**LEONARDO POLLINI** (Graduate Student Member, IEEE) received the B.Sc. and M.Sc. degrees in aerospace engineering from Politecnico di Torino, in 2018 and 2021, respectively. He is currently pursuing the Ph.D. degree within a Marie Curie European Industrial Doctorate Program in collaboration with the Politecnico di Torino, Turin, Italy, and Thales DMS, Élancourt, France.

His research interests lie in the field of computational electromagnetics. His focus areas include global optimization algorithms for flat antenna design, and automatic synthesis of metasurface antennas

**MARCELLO ZUCCHI** (Member, IEEE) received the B.Sc. degree in electronics and telecommunications engineering from the University of Bologna, Bologna, Italy, in 2014, the M.Sc. degree in electronics engineering and the Ph.D. degree in electrical, electronics and communications engineering from Politecnico di Torino, Turin, Italy, in 2018 and 2022, respectively.

In 2023, he joined the Department of Electronics and Telecommunications, Politecnico di Torino, as a Postdoctoral Researcher. Since June 2025, he has been a Researcher with the Advanced Computing, Photonics & Electromagnetics Area at Fondazione LINKS, Turin. His research interests include global optimization algorithms for flat antenna design, automatic synthesis of metasurface antennas, and field focusing algorithms for hyperthermia treatment.

**GIUSEPPE VECCHI** (Life Fellow, IEEE) received the Laurea and Ph.D. degrees in electronic engineering from the Politecnico di Torino, Turin, Italy, in 1985 and 1989, respectively.

He was a Visiting Scientist with Polytechnic University of NY from 1989 to 1990. Since 1990, he has been with the Department of Electronics, Politecnico di Torino, as an Assistant Professor, an Associate Professor from 1992 to 2000, and has been a Professor since 2000. He was a Visiting Scientist with the University of Helsinki, Helsinki, Finland, in 1992, and was an Adjunct Faculty with the Department of Electrical and Computer Engineering, University of Illinois at Chicago, Chicago, IL, USA, from 1997 to 2011. Since 2015, he has been serving as the Director with the Antenna and EMC Laboratory, Politecnico di Torino. He carried out hid doctoral research partly with Polytechnic University, Farmingdale, NY, USA. His current research activities concern analytical and numerical techniques for design, measurement and diagnostics of antennas and devices, medical applications, and imaging.

Prof. Vecchi is a member of the Board of the European School of Antennas and the IEEE Antennas and Propagation Standard Committee. He has been an Associate Editor of the IEEE TRANSACTIONS ON ANTENNAS AND PROPAGATION, the Chairman of the IEEE AP/MTT/ED Italian joint Chapter, and a member of the IEEE-APS Educational Committee.